PHYSICAL REVIEW D **88,** 083521 (2013)

Dark matter and pulsar model constraints from Galactic Center Fermi-LAT gamma-ray observations

Chris Gordon and Oscar Macías

Department of Physics and Astronomy, Rutherford Building, University of Canterbury, Private Bag 4800, Christchurch 8140, New Zealand

(Received 1 July 2013; published 21 October 2013)

Employing Fermi-LAT gamma-ray observations, several independent groups have found excess extended gamma-ray emission at the Galactic Center (GC). Both annihilating dark matter (DM) or a population of $\sim 10^3$ unresolved millisecond pulsars (MSPs) are regarded as well-motivated possible explanations. However, there are significant uncertainties in the diffuse galactic background at the GC. We have performed a revaluation of these two models for the extended gamma-ray source at the GC by accounting for the systematic uncertainties of the Galactic diffuse emission model. We also marginalize over point-source and diffuse background parameters in the region of interest. We show that the excess emission is significantly more extended than a point source. We find that the DM (or pulsar-population) signal is larger than the systematic errors and therefore proceed to determine the sectors of parameter space that provide an acceptable fit to the data. We find that a population of 1000–2000 MSPs with parameters consistent with the average spectral shape of Fermi-LAT measured MSPs is able to fit the GC excess emission. For DM, we find that a pure $\tau^+\tau^-$ annihilation channel is not a good fit to the data. But a mixture of $\tau^+\tau^-$ and $b\bar{b}$ with a $\langle\sigma v\rangle$ of order the thermal relic value and a DM mass of around 20 to 60 GeV provides an adequate fit.

DOI: 10.1103/PhysRevD.88.083521 PACS numbers: 95.35.+d, 98.80.−k

I. INTRODUCTION

There is considerable evidence that the majority of the matter in the Universe consists of cold dark matter (DM) rather than Standard Model particles [1–4]. Although there are many dark matter candidates, one of the most strongly motivated are weakly interacting massive particles (WIMPs). Prompt production, as well as decays, hadronization and radiative processes associated with the annihilation of WIMPs could result in a measurable signal of gamma-ray photons which may be observable by the Large Area Telescope (LAT) aboard the Fermi Gamma-Ray Space Telescope [5]. A promising location to search for WIMP annihilations is the central region of the Milky Way as it is relatively close by and has a high density of DM. However, the Galactic Center (GC) region also contains a large number of bright astrophysical sources. In particular, the interaction of energetic cosmic rays with the interstellar gas constitutes the main source of Galactic diffuse emission. Unfortunately, there is significant uncertainty about the propagation and origin of these cosmic rays, the distribution of the magnetic fields, radiation fields and the interstellar medium. In addition, due to the relatively low angular resolution of the LAT instrument ($\sim 0.2°$ at 10 GeV), several undetected point-like gamma-ray sources could mimic diffuse gamma-ray emission; consequently, the task of disentangling a tentative DM signal from the astrophysical background necessarily implies the implementation of detailed techniques to account for the uncertainties of the Galactic diffuse emission model.

The GC hosts a supermassive black hole with a mass of $\sim 4 \times 10^6 M_\odot$, called Sagittarius A* (Sgr A*). With the Fermi-LAT resolution, it can be modeled as a point source with a curved spectral shape [6]. The interesting analysis performed in Ref. [7] points out that the upcoming Cherenkov Telescope Array will be key in the understanding of the physical mechanisms powering high-energy photons from Sgr A*.

Constraints on annihilating DM have been made using dwarf galaxies [8,9] and galaxy clusters (e.g., Refs. [10–12]). Several studies have found an excess of gamma rays in the GC that are consistent with roughly a 10–100 GeV DM mass annihilating into $\tau^+\tau^-$, $b\bar{b}$ final states or a combination of both [13–18]. The Fermi-LAT Collaboration have not yet published a full analysis of GC excess, but a preliminary study by them using one year of data reported an excess in observed counts around energies of 2–5 GeV [19,20] at the GC.

The signal was also shown to be consistent with a population of millisecond pulsars (MSPs) in the GC [17,18,21]. Studies have also looked at the possibility of the signal arising from cosmic-ray interaction with gas in the GC [7,16–18,22]. The authors of Refs. [17,18] highlighted the need to marginalize over the point source (PS) parameters, due to their degeneracy with any proposed model for the excess GC emission.

In this article we extend the treatment of Refs. [17,18] in a number of ways. In particular we estimate systematic errors for the galactic diffuse background. We also evaluate marginalized confidence intervals and determine the areas of parameter space that provide an acceptable fit to the

data. In Sec. II we describe the data used and some initial goodness of fit tests. In Sec. III we check the spatial fit of the models and evaluate the systematic errors in the diffuse Galactic background. The results are given in Sec. IV and the discussion and conclusions are given in Secs. V and VI, respectively.

II. FERMI-LAT OBSERVATIONS AND DATA REDUCTION

A detailed description of the characteristics and performance of the LAT instrument aboard Fermi is given in Ref. [23]. The LAT data used in this work were collected for about 45 months of continuous sky-survey observations over the period August 4, 2008–June 6, 2012 [corresponding to mission elapsed time 239557417–360716517]. The SOURCE event class was chosen and photons beyond the Earth zenith angle of 100° were excluded to minimize Earth albedo gamma rays. Time periods during which the spacecraft rocking angle is larger than 52° are also excluded as an additional guard against gamma-ray contamination. We further restrict the analysis to the photon energy range 200 MeV–100 GeV and make no distinction between *Front* and *Back* events.

We select all events within a squared region of interest (ROI) of size $7° \times 7°$ centred on $(\alpha, \delta) = (266°.417, -29°.008)$. This position coincides with the current best-fit coordinates of the gamma-ray source 2FGLJ1745.6-2858 (Sgr A*). The analysis is performed using the LAT Science Tools package V9R27P1 and the P7_V6 instrument response functions (IRFs).

We model the Galactic background component using the LAT standard diffuse background model GAL_2YEARP7V6_V0.FITS. The extragalactic and residual instrumental backgrounds, assumed as being isotropic, are fitted with the file ISO_P7V6SOURCE.TXT.

The analysis of the Fermi-LAT spectrum was performed using a binned likelihood technique [24] with the *pyLikelihood* library in the Science Tools. The energy binning was set to 20 logarithmic evenly spaced bins.

We adopted the same fitting procedure followed in Refs. [17,18]. This is a relaxation method which consists in freeing the spectral model parameters consecutively from their distance to Sgr A*. Normalizations are freed first, and then the full spectra within concentric regions: within 2°, then within the $7° \times 7°$ square region and finally in the full ROI and for all sources whose $TS > 25$, with the test statistic (TS) defined as in Ref. [6],

$$TS = 2[\log \mathcal{L}(\text{new source}) - \log \mathcal{L}(\text{NO-new source})], \quad (1)$$

where $\mathcal{L}$ stands for the maximum of the likelihood of the data given the model with or without the new source at a certain location of the ROI. In the large-sample limit, under the no-source hypothesis, TS has a $\chi^2/2$ distribution with the number of degrees of freedom equal to the number of parameters associated with the proposed positive-amplitude new source [24,25], which in this case is two for position, one for amplitude, and one for spectral slope, so four in total. As the amplitude is restricted to be

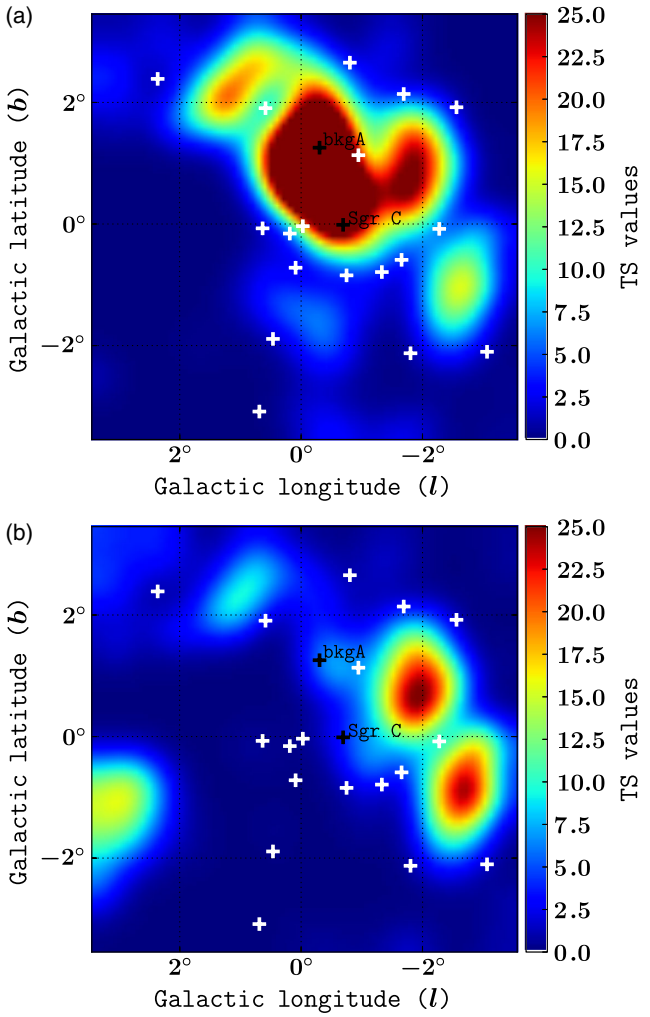

FIG. 1 (color online). Residual TS maps in the energy range 300 MeV–100 GeV for two different best-fit models of the Galactic Center region using (a) only the known 2FGL point and extended sources (baseline model), highlighted here with white crosses, and (b) the full set of 2FGL sources plus the best-fit spatial and spectral model of an extended source at the Galactic Center (lower panel) (see Sec. III for details on maps for the extended source). The two black crosses show the localization of two recently proposed gamma-ray PSs [22] named BKGA and SGR C, whose significance drops drastically once the extended source has been taken into consideration. This can be seen in the bottom figure. The maps span a $7° \times 7°$ region of the sky centered at the Sgr A* position and the extent of every pixel is $0.1° \times 0.1°$. The residual TS maps have been smoothed for display with a $\sigma = 0.3°$ Gaussian. For display purposes the images have been thresholded at $TS = 25$.

TABLE I. Point-source candidates found in the GC field of view for almost four years of Fermi-LAT data. The PS detection and localization were carried out following the same approach explained in Ref. [12].

Right ascension [deg]	Declination [deg]	TS
264.813	−30.270	70.8
265.735	−31.814	65.1

non-negative, a $\chi^2/2$ distribution rather than the χ^2 distribution is needed.

Using the MAKE2FGLXML.PY tool we generated all the relevant second-year Fermi catalog (2FGL) sources that could contribute to the ROI and applied to it the aforementioned relaxation method: this is called the "baseline" model [17,18].

A. Detection of an extended source at the Galactic Center

In order to evaluate to what extent the data prefers a model that considers GC excess extended emission instead of the conventional one assumed in the 2FGL [6], we have constructed two residual TS maps shown in Fig. 1. For a given pixel in the map, a trial new PS is added with a power-law spectrum and its TS is evaluated. The usual convention [6] is to investigate the possibility of a new PS if $TS \geq 25$ for PSs far from the Galactic Plane. In producing the TS images, we made use of the

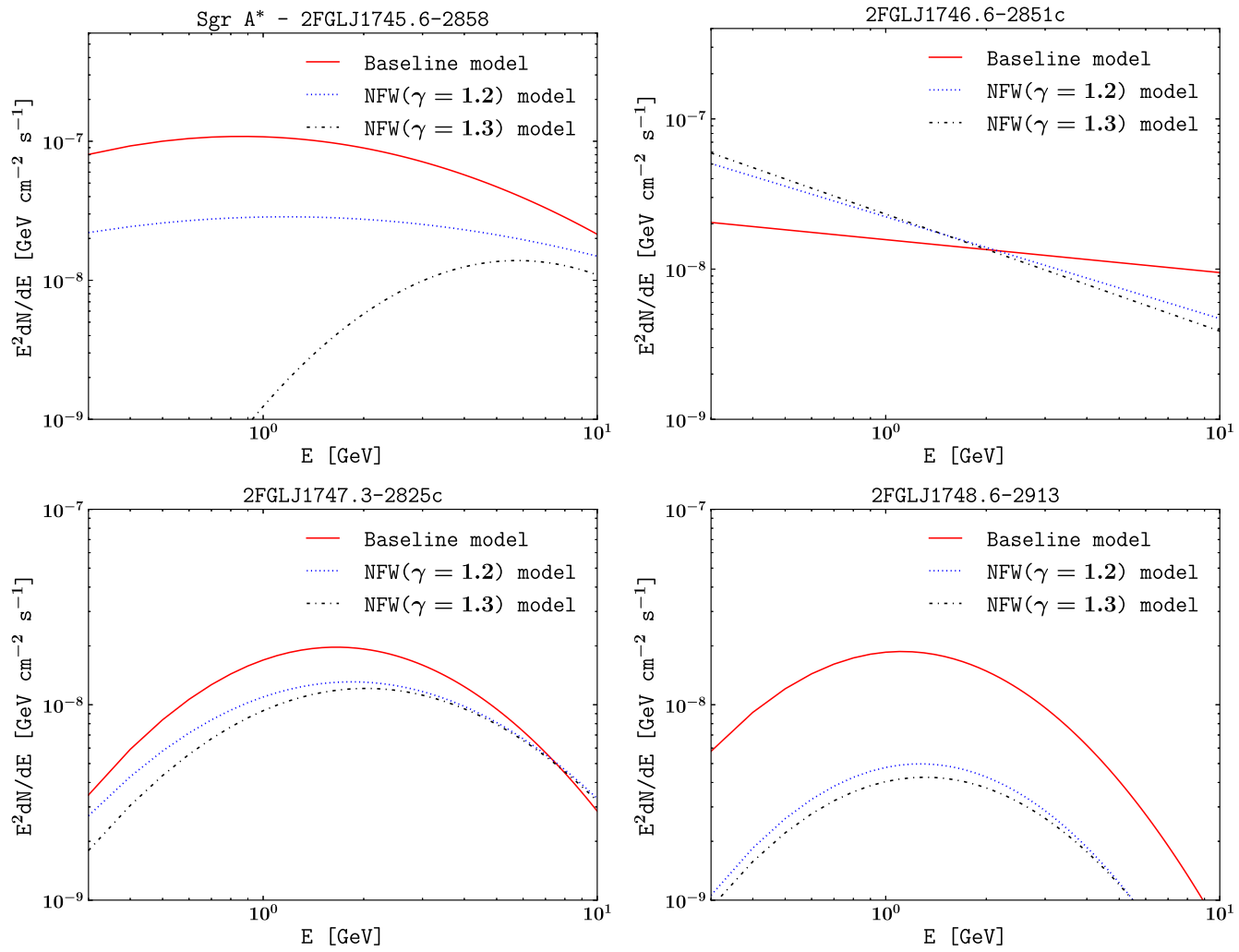

FIG. 2 (color online). Shown is the spectrum of the four 2FGL PSs displaying the largest degeneracy pattern as obtained from three different fits. The continuous red line shows the spectrum for each source that we get from our baseline model (i.e. a model that just assumes the conventional 2FGL sources). The blue dotted and black dash-dotted lines exhibit the source's spectra when the newly discovered extended source at the GC is included. This extended source is modelled with spatial maps following a universal NFW profile with inner slopes $\gamma = 1.2$ and $\gamma = 1.3$, respectively (see details on maps in Sec. III). The spectra of the extended source is modelled with a log parabola for both cases. The source's spectra shown here are organized in order of their proximity to the central position from left to right and top to bottom and all of them are located within 1° of the center of the ROI.

Fermi Science Tool GTTSMAP, as recommended in the CICERONE.[1]

We notice that by including the new best-fitting spatially extended source [Fig. 1(b)] the ROI integrated TS of the map decreased by 48% relative to a fit with no GC extended source [Fig. 1(a)]. The inclusion of an GC extended source typically has a TS of order 800 and so it is very significantly favored by the data. In Ref. [22] two new PSs named BKGA and SGR C, were claimed to have been discovered. In fact, our analysis shows that once the more adequate extended source is included, their significance fades in the Fermi-LAT data. Nevertheless, the effect that these two new PSs had on the extended-source hypothesis was evaluated in Refs. [17,18], where a negligible variation in the main conclusions was found. We therefore do not attempt to model these sources in this article.

A visual inspection of the TS image shown in Fig. 1(b) suggests that the residuals can be further ameliorated by including two new PSs at the coordinates listed in Table I. However, based on the examination of the sources near Cygnus, Orion and molecular clouds, the Fermi collaboration [6] stipulated that depending on the intensity of the diffuse background, sources near the Galactic Ridge need to have $TS \gg 25$ to not be considered diffuse features.

We calculated the background photon count per pixel $N_{\rm bkgd}$ by integrating the diffuse model cube for our ROI from 589 MeV to 11.4 GeV and found an average of $N_{\rm bkgd} = 42.2$ (where each pixel spans an area of $0.1^\circ \times 0.1^\circ$). According to this source-detection criteria, a new source would need to have a $TS \gtrsim 80$ to be seriously considered for a multiwavelength search. We therefore do not claim the discovery of new PSs in the field of view.

Interestingly, in a recent study of the Virgo cluster [26], the detection of extended gamma-ray emission was interpreted as dark matter annihilation. That hypothesis was later disputed in Ref. [12] where it was argued that a set of previously unknown PSs or features of the diffuse background could have accounted for the majority of the excess emission. This was later confirmed in Ref. [27].

We undertake here the same approach as in Ref. [12] and evaluate the new significance of the excess emission when the PSs in Table I are included. However, contrary to what happened in the Virgo case [12], we find that the TS and flux of the extended source at the GC were mildly enhanced (see details in Sec. III).

In the innermost region of the GC (a circular area with a radius of about 1° centred on Sgr A*) the spectral parameters describing the gamma-ray sources are degenerate with the extended source parameters [17,18]. This means that when the new extended gamma-ray source is not considered in the analysis [Fig. 1(a)], the four nearest sources to the central position are assigned a larger amplitude to account for the excess emission [17,18]. This phenomena can be seen in Fig. 2, where the behavior of the four sources in the innermost region is depicted.

[1] http://fermi.gsfc.nasa.gov/ssc/data/analysis/documentation/Cicerone/.

III. MORPHOLOGY OF THE EXTENDED SOURCE

A. Dark matter and pulsar maps

The gamma-ray flux emitted by WIMP interactions with mass $M_{\rm DM}$ can be factorized [28–30] into two conceptually distinct terms: (i) a "particle physics factor" $\Phi^{\rm PP}(E_\gamma)$ that accounts for the number of gamma-ray photons produced per annihilation event at a given photon energy, and (ii) an "astrophysical factor" $J(b, l)$, which measures the number of dark matter particle pairs producing photons along the line-of-sight direction. That is,

$$\Phi(E_\gamma, b, l) = \Phi^{\rm PP}(E_\gamma) \times J(b, l), \tag{2}$$

where b and l are the Galactic latitude and longitude, respectively. The particle physics contribution is often written as

$$\Phi^{\rm PP}(E_\gamma) = \frac{1}{2}\frac{\langle\sigma v\rangle}{4\pi M_{\rm DM}^2}\sum_f \frac{dN_f}{dE_\gamma}B_f, \tag{3}$$

where $\langle\sigma v\rangle$ is the annihilation cross section of two DM particles times their relative velocity, averaged over the velocity distribution. dN_f/dE_γ is the differential gamma-ray multiplicity per annihilation, B_f is the branching ratio and f stands for the final-state particles resulting from the annihilation.

The astrophysical factor in the (b, l) direction is integrated over the line of sight [30],

$$J(b, l) = \int_0^\infty ds\rho(r)^2|_{r=\sqrt{R_\odot^2 - 2sR_\odot\cos(b)\cos(l)+s^2}}, \tag{4}$$

with s varying in the line-of-sight path, and $R_\odot = 8.25$ kpc is the distance from the solar system to the GC. Since the spatial binning of our Fermi files was $0.1^\circ \times 0.1^\circ$, we constructed the spatial maps by averaging the astrophysical factor over the corresponding solid angle around the (b, l) coordinates [30],

$$\langle J(b, l)\rangle_{\Delta\Omega} = \frac{1}{\Delta\Omega}\int_{\rm pixel} J(b, l)d\Omega, \tag{5}$$

where the differential solid angle is given by $d\Omega = db\, dl\cos(b)$.

As in Refs. [17,18], throughout this work we shall use template maps of DM that assume a generalized Navarro-Frenk-White (NFW) profile [31,32],

$$\rho(r) = \frac{\rho_s}{(\frac{r}{r_s})^\gamma[1 + (\frac{r}{r_s})^\alpha]^{(\beta-\gamma)/\alpha}}, \tag{6}$$

where we fix $r_s = 23.1$ kpc, $\alpha = 1$, and $\beta = 3$.

It has been suggested that the excess emission seen in the GC can also be explained by a superposition of unresolved

PSs (such as MSPs) that might be distributed as a mildly contracted NFW profile. We tested this hypothesis by normalizing to unity the $\langle J(b,l)\rangle$ maps, as explained in the CICERONE.[2]

These normalized maps were also used to fit for the inner slope γ. This was done with two equivalent methods:

(i) We first computed the residual emission shown in Fig. 3. From this we produced a radial profile [Fig. 4(a)] of the photon excess. This was compared with that expected from a PS and also from well-motivated spatially extended sources using a χ^2 test. The profiles for the extended source shown in the histograms in Fig. 4(a) were obtained with the GTMODEL routine. The models entered into this tool were $\langle J(b,l)\rangle$ maps normalized to unity with $\gamma \in [1.0, 1.5]$ and a log-parabola spectra,

$$\frac{dN}{dE} = N_0\left(\frac{E}{E_0}\right)^{-(\alpha+\beta\log[\frac{E}{E_0}])}. \quad (7)$$

The height of each bin is given by the mean of the residual in a ring of pixels centered around the GC. The error bars were evaluated as the standard deviation of the pixels in the ring divided by the square root of the number of pixels in the ring.

(ii) Following a more statistically robust approach we proceeded to fit for γ with the *pyLikelihood* tool [Fig. 4(b)]. Compared to the previous method, this one has the advantage of carefully considering the energy binning in the likelihood function.

As we are using the profile likelihood approach [33], we set $\gamma = 1.2$ unless otherwise specified. Although ideally one should maximize the likelihood for γ simultaneously with the other parameters, our initial tests show that the preference for $\gamma = 1.2$ is robust to changes in the spectral model. Also, when maximizing the likelihood of the microlensing and dynamical data (see Fig. 5 of Ref. [34]), $\gamma = 1.2$ corresponds to $\rho_0 \equiv \rho(R_\odot) = 0.36\ \mathrm{GeV\,cm^{-3}}$. From Eqs. (2)–(4) and (6) the annihilation gamma-ray flux is $\Phi \propto \langle\sigma v\rangle\rho_0^2$, and so ρ_0 is not constrained by the Fermi-LAT measurements alone. Also, the microlensing and dynamical data impose a very weak constraint on γ compared to our Fermi-LAT analysis, and so this justifies using the Fermi-LAT best-fit value for γ in constraining ρ_0.

The microlensing and dynamical data constrain the scale radius to be $r_s = 20^{+15}_{-10}$ kpc [34]. As this is much larger than the extent of the excess emission (200 pc), the gamma-ray data is not able to constrain r_s. But, as can be seen from Eqs. (4) and (6), r_s may affect J and it will also be completely degenerate with $\langle\sigma v\rangle$. In line with the profile likelihood approach, we choose r_s to be consistent with the maximum likelihood value given in Ref. [34]. It would be better to use the maximum likelihood value of r_s when γ is fixed to 1.2, but the joint confidence intervals for r_s and γ are not given in Ref. [34]. Our current approach should provide a reasonable approximation unless the microlensing and dynamical data have a very high correlation in the joint confidence intervals for r_s and γ.

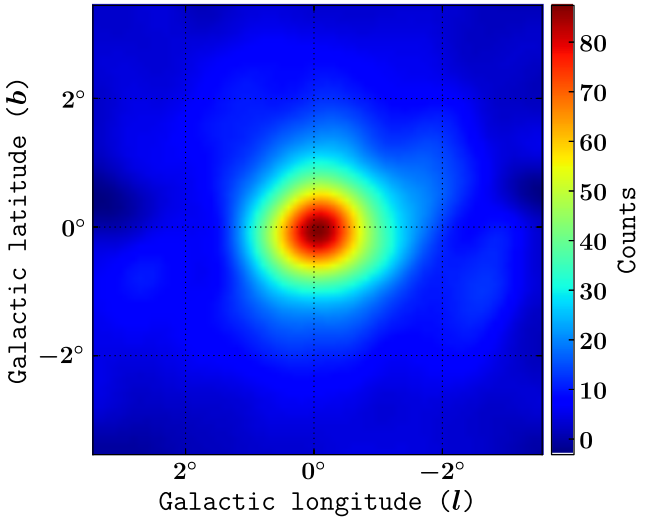

FIG. 3 (color online). LAT residual map after the subtraction of our best-fit model with an extended GC source, but without subtracting the extended source model component. The counts were summed over the energy range 300 MeV–10 GeV. The map spans a $7° \times 7°$ region of the sky centred at the Sgr A* position with a pixel size of $0.1° \times 0.1°$. The residual has been smoothed with a $\sigma = 0.3°$ Gaussian.

As it has been seen in Figs. 4(a) and 4(b), comparisons between LAT point spread functions (PSFs) and photon distributions indicate that the observed excess emission is consistent with an extended source whose spatial distribution is well described by a mildly contracted NFW profile. Below we outline how we examined its spectral morphology for a DM hypothesis.

We calculated the gamma-ray spectra from WIMP self-annihilations with the DMFIT tool as described in Ref. [35]. This package provides interpolating functions calculated from simulations of DM annihilations with the DARKSUSY software [36], which in turn interpolates over PYTHIA 6.4 [37] tables.

It has recently been pointed out that there are discrepancies [38] between the gamma-ray spectra calculated with PYTHIA 6.4 (Fortran version) and PYTHIA 8.1 [39] (C++ version), namely that software analysis using interpolating functions can overestimate the energy cutoff of the gamma-ray spectra [40], and that not considering electroweak corrections can also create deviations between predicted DM annihilation spectra [41,42]. We therefore looked for a statistical bias in our analysis by producing PYTHIA 8.1 tables for a few WIMP masses and found that for the relevant energy scale and annihilation channels used in

[2] http://fermi.gsfc.nasa.gov/ssc/data/analysis/scitools/extended.

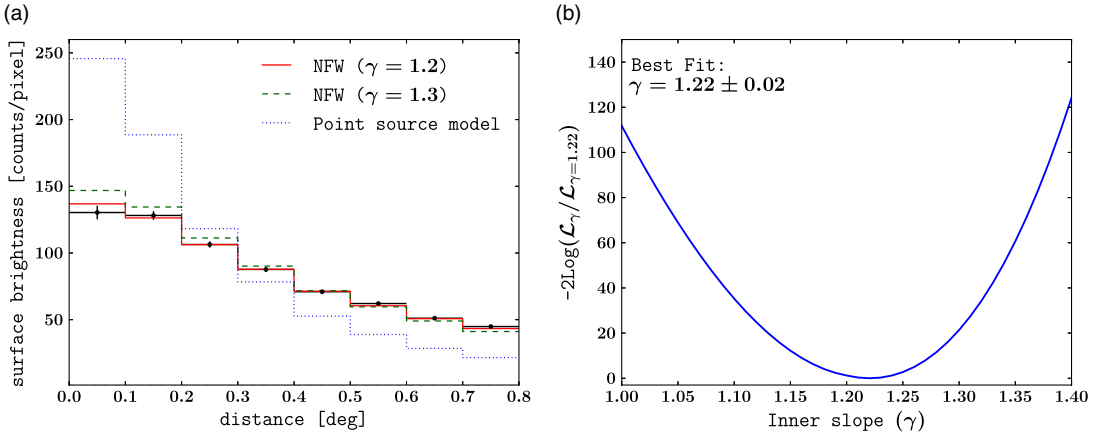

FIG. 4 (color online). (a) Radial profile of the LAT residuals shown in Fig. 3 as obtained from a ring analysis computed around Sgr A*. The histograms show the effective LAT PSF for three different profile models: (i) NFW with inner slope $\gamma \simeq 1.2$ (red continuous line), for which we get $\chi^2/\text{d.o.f.} = 5.5/7$; (ii) NFW with $\gamma = 1.3$ (green dashed line) and $\chi^2/\text{d.o.f.} = 44.6/7$; (iii) the profile for a PS model (blue dotted line) with $\chi^2/\text{d.o.f.} = 2479.9/7$. For all cases the spectra was modelled with a log parabola. (b) Shown is the significance of NFW profiles with varying inner slope, where $\mathcal{L}_\gamma$ represents the likelihood function at a given γ. This was assessed by performing set Fermi Tools runs where for each case the relaxation method was used. The spectra was fitted with a log-parabola function and only statistical uncertainties were taken into account.

our work the discrepancies between the results obtained with DMFIT and PYTHIA 8.1 were marginal.

For the DM spectrum we considered soft gamma-ray spectra produced from annihilation into $b\bar{b}$ quarks and hard spectra as produced by annihilations into $\tau^+\tau^-$ or a combination of lepton pairs (e^+e^-, $\mu^+\mu^-$ and $\tau^+\tau^-$). Since the annihilation products are highly model dependent we studied extremes of the possible annihilation channels assuming a branching ratio of 100% for each of them in turn (except for the case of 100% e^+e^-), but mixtures of soft and hard spectra were also evaluated in order to fit for the best branching ratio B_f.

B. Examination of systematics in the Galactic diffuse background model

The LAT team developed a model for the Galactic diffuse background map which is an essential input to the analysis for detecting and characterizing gamma-ray sources. The model file GAL_2YEARP7V6_V0.FITS introduced in the 2FGL catalog [6] was created by fitting all-sky gamma-ray data with a highly sophisticated physical model. In a nutshell, the distribution of interstellar gas and dust was obtained from independent observations, and then three-dimensional models of magnetic fields, distributions of optical photons and models of p and e^- injections were assumed. By propagating these primary particles through the gas with the GALPROP[3] software package, the resulting photons from inverse Compton scattering, bremsstrahlung and π^0 decays were predicted and fitted with gamma-ray data.

Since the newly discovered extended source is located in the region where the Galactic diffuse background component largely dominates over any other sources, we therefore expect the uncertainties[4] associated with the Galactic diffuse background model to constitute the largest systematic effects for the analyses in this study.

In order to estimate the uncertainties of the Galactic diffuse background at the GC, we would like to examine a region of the sky which has a similar Galactic diffuse background as the GC but does not contain any other sources that would also contribute to the residuals. As argued in Ref. [43], the Galactic diffuse background has relatively similar uncertainties within the inner Galaxy ($-80° \geq l \leq -80°$, $-8° \leq b \geq 8$). Based on these considerations, we estimate the percentage uncertainties from nearby regions along the Galactic plane which do not have any point sources.

We first examined the spectral uncertainties by obtaining the energy dependence of our model residuals. Following a similar approach to that explained in Ref. [44], we compared the observed counts with the model counts in a nearby circular region with a radius of 0.5° centred on $\Delta l \sim +2.3°$ and $\Delta b \sim 0°$ where the Galactic diffuse background component was found to be dominant; see Fig. 5(a). The "model counts" map was computed from our best-fit model (i.e. the baseline model plus an NFW distributed source with $\gamma = 1.2$ and log-parabola spectra). This step is summarized in Fig. 5(b), where the residuals as a function of energy are shown.

[3] http://galprop.stanford.edu.

[4] The uncertainties are mainly due to contributions of unresolved PSs and imperfections of the Galactic diffuse background model.

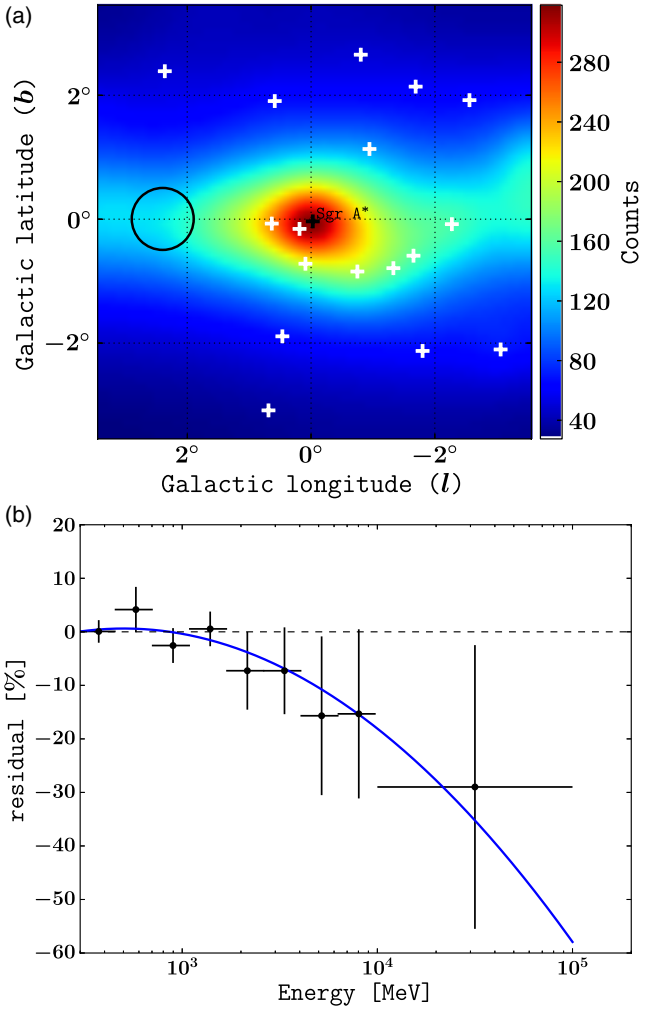

FIG. 5 (color online). (a) Counts map in the 0.3–100 GeV energy band of the best-fit model for the ROI. This model considers the conventional 2FGL sources plus an additional extended source at the central position (see details in Sec. III A). Gaussian smoothing is applied with a kernel size of $\sigma = 0.3°$. The black circle superposed on the image shows a region dominated by the Galactic diffuse background that was used to examine the spectral uncertainties. (b) Fractional residuals—that is (observed-model)/model—evaluated at eight energy bins in a circle centered at $(l, b) = (+2.3°, 0°)$ with a radius of 0.5°, as shown in the above image. The residual data was fitted with a quadratic function on a logarithmic scale, as described by the blue line.

In order to assess the spatial uncertainties of the Galactic diffuse background component, we quantified the dispersion of the fractional residuals in ten regions where the Galactic diffuse background component was found to be dominant. The regions selected are located in the Galactic plane and special emphasis was put on not considering sectors with known 2FGL PSs within them. The fractional residual for each region was calculated in five energy bands: 0.30–0.50 GeV, 0.50–0.80 GeV, 0.80–1.30 GeV, 1.3–10 GeV and 10–100 GeV. The results obtained in this step are shown in Fig. 6. It follows that the standard deviation of the fractional residuals is 11%. We thus used this value as an estimate of the uncertainties in the spatial distribution of the Galactic diffuse background component. A similar magnitude for the spatial and spectral uncertainties was found in Ref. [44], which was also in the inner Galaxy.

The spectral and spatial uncertainties described above will be used in Sec. III C to estimate the systematic error in the flux of the extended source.

C. Spectral morphology of the extended source

The procedure of obtaining the spectral energy distribution (SED) of the extended source was based on the method used for the flux-band analysis in Ref. [6]. We started by applying the relaxation method (explained in Sec. II) to the ROI in the full energy range of 0.3–100 GeV. The extended source was modeled with an NFW ($\gamma = 1.2$) map normalized to unity and the spectra were modeled with a log parabola formula, as defined in Eq. (7). Once the best-fit spectral parameters $\alpha(E_0)$ and β were found, we calculated the spectral slope of the log parabola at any given energy as

$$\alpha(E) = \alpha(E_0) + 2\beta \log\left(\frac{E}{E_0}\right), \tag{8}$$

where E_0 is the pivot energy [6].

We divided the energy range of the extended source into 12 energy bands evenly separated in the range 0.3–10 GeV and one energy band from 10 GeV to 100 GeV. Next, the extended-source photon fluxes in each band were computed by freezing the spectral indexes of all the 2FGL sources to those obtained in the fit over the full range and by fitting the normalizations in each spectral band. Note that the diffuse galactic and extragalactic backgrounds were not frozen and neither were the PS amplitudes: they were optimized along with each band amplitude. In an initial analysis we had also included a 200–300 MeV band but we found it had a TS of only 0.4, so we did not include it in our further analysis. Also, the extended-source models generally have a negligible amplitude in the 200–300 MeV band compared to Sgr A*. For each remaining energy band, the GC extended-source spectrum was approximated by a power-law function,

$$\frac{dN}{dE} = N_0\left(\frac{E}{E_0}\right)^{-\Gamma}, \tag{9}$$

where the spectral index Γ in a band was set to the local spectral slope defined in Eq. (8) at the logarithmic midpoint of the band $\sqrt{E_n E_{n+1}}$, restricted to be in the interval [0, 5]. We calculated 2σ upper limits instead of actual fluxes for those bands with either a test statistic $TS < 10$ or a relative uncertainty in the flux $\Delta F_i/F_i > 0.5$.

Systematic errors due to uncertainties in the Galactic diffuse background model were evaluated by modifying

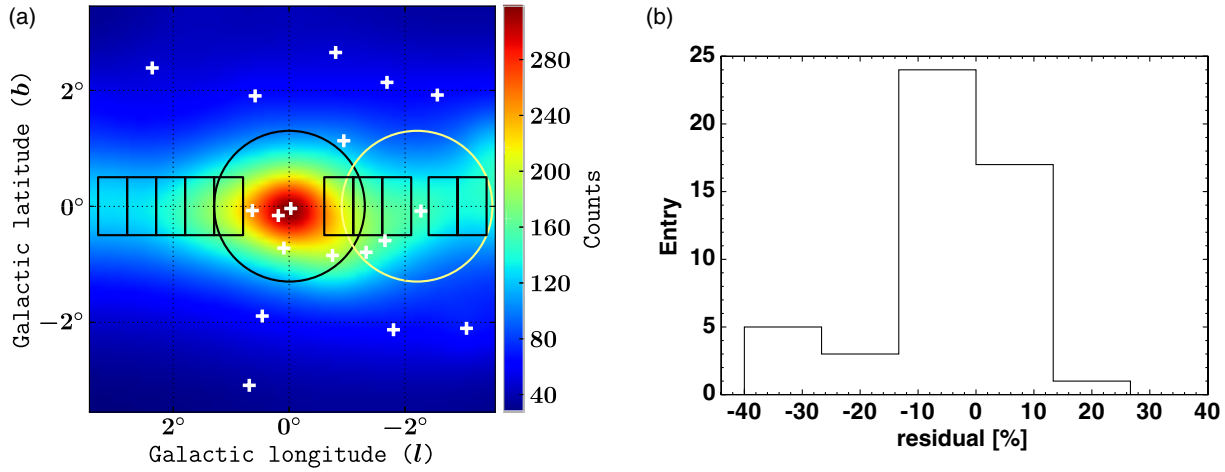

FIG. 6 (color online). (a) Counts map in the 0.3–100 GeV energy band smoothed with a Gaussian filter of radius $\sigma = 0.3°$. The black rectangles ($1.0° \times 0.5°$) highlight the regions selected for the examination of the spatial uncertainties in the Galactic diffuse background. The black and yellow circles show the regions where the flux of the file GAL_2YEARP7V6_V0.FITS was varied to evaluate the effects of the spatial dispersion of the model. (b) Histogram of the fractional residuals for ten rectangular regions in five energy bands: 0.30–0.50 GeV, 0.50–0.80 GeV, 0.80–1.30 GeV, 1.3–10 GeV and 10–100 GeV. The residuals were calculated as (observed-model)/model, where we also subtracted the best-fit fluxes of all the sources (except for the Galactic diffuse background source) from the observed counts map.

the model file GAL_2YEARP7V6_V0.FITS in the band analysis. This was done differently for spectral and spatial uncertainties:

(i) To calculate the spectral uncertainties we performed an additional band analysis where we altered the energy distribution of the Galactic diffuse background model according to the curve in Fig. 5. We thus compared the fit with and without this modification and set the spectral systematic error to be the difference between the two.

(ii) Spatial uncertainties were estimated using two modified GAL_2YEARP7V6_V0.FITS files in the fit. For all energy bins in the model cubes, we varied the fluxes by 11% in first a disk of radius 1.3° centred on Sgr A*, and then an offset disk at $(b, l) = (0°, 2.1°)$ with the same dimensions. Again, after a comparison of both fits we chose the one with the largest uncertainties to be included in our SED calculation. Both disks are illustrated in Fig. 6(a).

The resulting systematic errors due to uncertainties of the spectral distribution in the Galactic diffuse background model were found to on average be about 2%, while for the spatial errors we obtained on average of about 20%, both values being for the energy ranges ≤ 10 GeV. For the 10 to 100 GeV band we found the systematic error to be of order 40%. Also, we find that in general the models that fit the ≤ 10 GeV range have negligible values in the higher than 10 GeV band. For these reasons we do not use the 10 to 100 GeV energy band.

Total systematic errors were computed by adding in quadrature the spatial, spectral and effective area systematics, which is explained below Eq. (10). In Fig. 7 we show the SED of the extended source overlaid with the best fit over the full range. The red error bars indicate the total systematic errors and black error bars indicate the statistical uncertainties. We also list the SED and errors in the Table V of Appendix so that the reader may try to fit other spectral models.

In order to study the validity of the distinct types of spectral shapes found with high TS values in our Fermi Tools runs, we used the same spectral-fit quality estimator introduced in Ref. [6] except that we also added our systematic errors for the diffuse Galactic background,

$$C_{\rm syst} = \sum_i \frac{(F_i - F_i^{\rm fit})^2}{\sigma_{i\,\rm stat}^2 + \sigma_{i\,\rm spatial}^2 + \sigma_{i\,\rm spectral}^2 + \sigma_{i\,\rm area}^2}, \quad (10)$$

where i runs over all bands with $TS > 10$, $F_i^{\rm fit}$ is the flux predicted in that band from the spectral fit to the full band, and the denominator contains a sum of the squares of the statistical error, the Galactic diffuse background spatial systematic error, the Galactic diffuse background spectral systematic error, and the effective area systematic error. Also, $\sigma_{i\,\rm area}^2 = (f_i^{\rm rel} F_i^{\rm fit})^2$, where $f_i^{\rm rel}$ represents the systematic uncertainty in the effective area [6]. The f_i were set to 0.05 for the first seven bands and 0.08 from bands eight to twelve. The first energy band situated in the range 300–400 MeV was found to have a $TS < 10$, and therefore it was not included in our analysis. We will assume that $C_{\rm syst}$ has a χ^2 distribution with the number of degrees of freedom equal to the number of bands

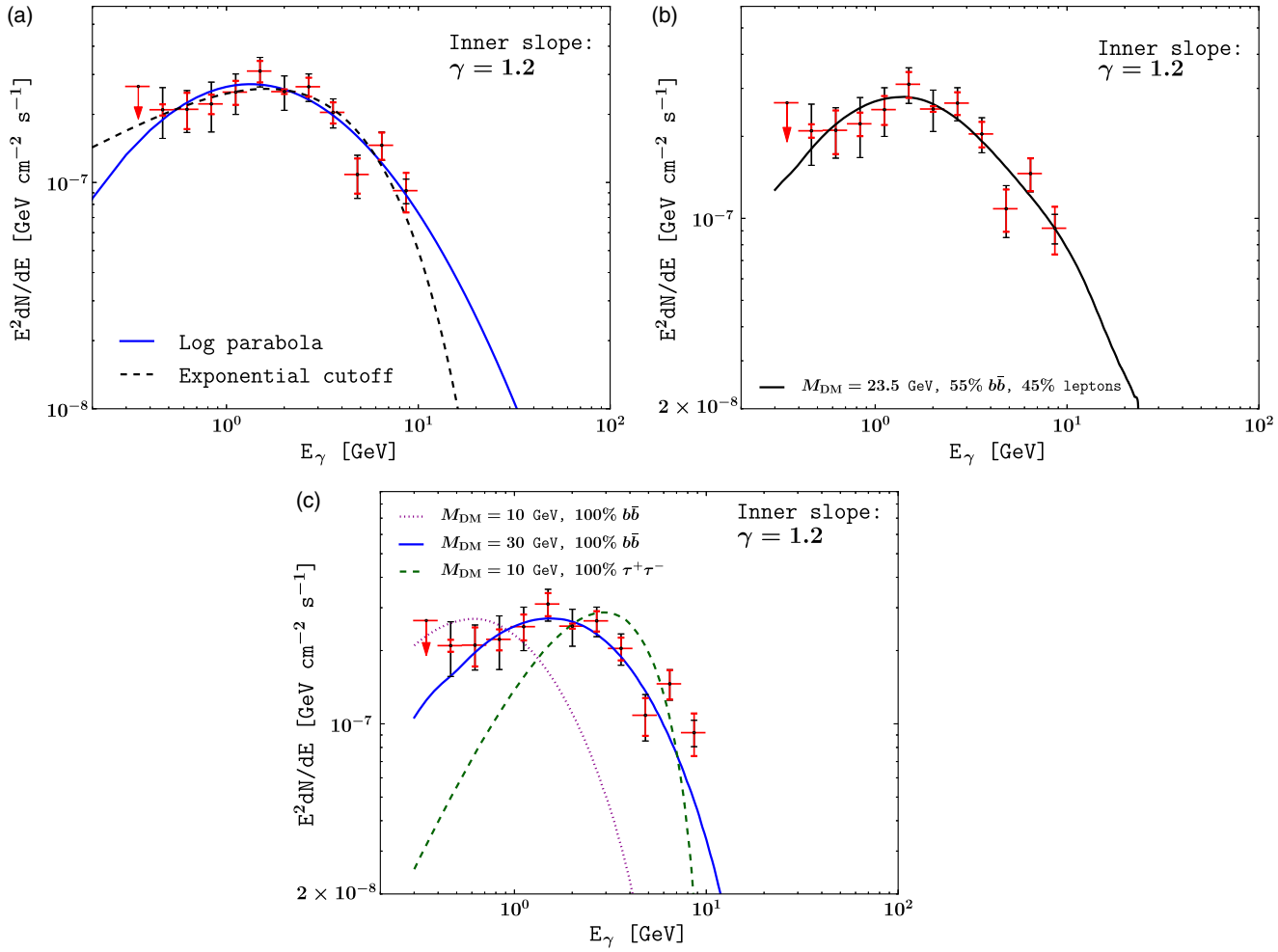

FIG. 7 (color online). Spectrum of the extended source measured with the Fermi-LAT. As shown in the legends, the model for the spatial distribution of the source is an NFW profile with inner slope $\gamma = 1.2$. The red and black error bars show the (1σ) systematic and statistical errors, respectively. The upper limit is 2σ. The fit over the full range is overlaid over the twelve-band energy fluxes on each figure as follows. (a) The continuous blue line and dashed black line represent the best-fit spectrum for a population of MSPs resembling an NFW spatial distribution; two typical curved spectra of these sources have been used. See text for details on the goodness of the fit. (b) Shown is the best-fit DM spectrum. M_{DM}, B_f and $\langle\sigma v\rangle$ were treated as free parameters in the fit. The black continuous line represents WIMPs of 23.5 GeV self-annihilating 55% and 45% of the time into quarks $b\bar{b}$ and leptons (here "leptons" denotes an unweighted mixture of e^+e^-, $\mu^+\mu^-$ and $\tau^+\tau^-$), respectively. (c) The figure shows three different examples of DM spectra with high TS values as obtained with Fermi Tools, where just $\langle\sigma v\rangle$ was allowed to vary in the fit. Although WIMPs of 10 GeV annihilating all the time into $\tau^+\tau^-$ or $b\bar{b}$ only satisfy the $TS > 25$ criteria, they in fact do not pass the goodness-of-fit threshold; see details in Sec. IV B. As it can be seen, $M_{DM} = 30$ GeV, 100% $b\bar{b}$ exemplifies a good-fitting model with significant curved spectra.

(that is, 11) minus the number of parameters used to determine $F_i^{\rm fit}$. Assuming that the systematic errors can be treated as independent and Gaussian distributed, this is a good approximation as we have a large number of counts for each band.

The goodness of fit can be evaluated from the p value, which is the probability of $C_{\rm syst}$ taking on a value larger than the observed value. We can evaluate the p value as $\int_{C_{\rm syst}}^{\infty} p(x)dx$, where $p(x)$ is a χ^2 distribution with degrees of freedom equal to 11 minus the number of parameters. The authors of Ref. [6] took a good fit to be one with a p value greater than 10^{-3}. For a two-parameter fit with 11 bands this corresponds to $C_{\rm syst} < 27.9$. For the three-parameter case this corresponds to $C_{\rm syst} < 26.1$.

In the first row of Fig. 7 we show examples of spectra with high TS values and significant curved spectral shapes for two well-motivated hypotheses: an unresolved population of MSPs in the GC, and dark matter self-annihilating into a mixture of $b\bar{b}$ quarks and leptons. Figure 7(c) shows examples of DM spectra proposed in the literature as good-fitting models for the GC gamma-ray excess. However, our analysis demonstrates that DM particles of $M_{DM} =$ 10 GeV annihilating into $\tau^+\tau^-$ or $b\bar{b}$ only do not fit the LAT data correctly, since they have $C_{\rm syst} \gg 27.9$.

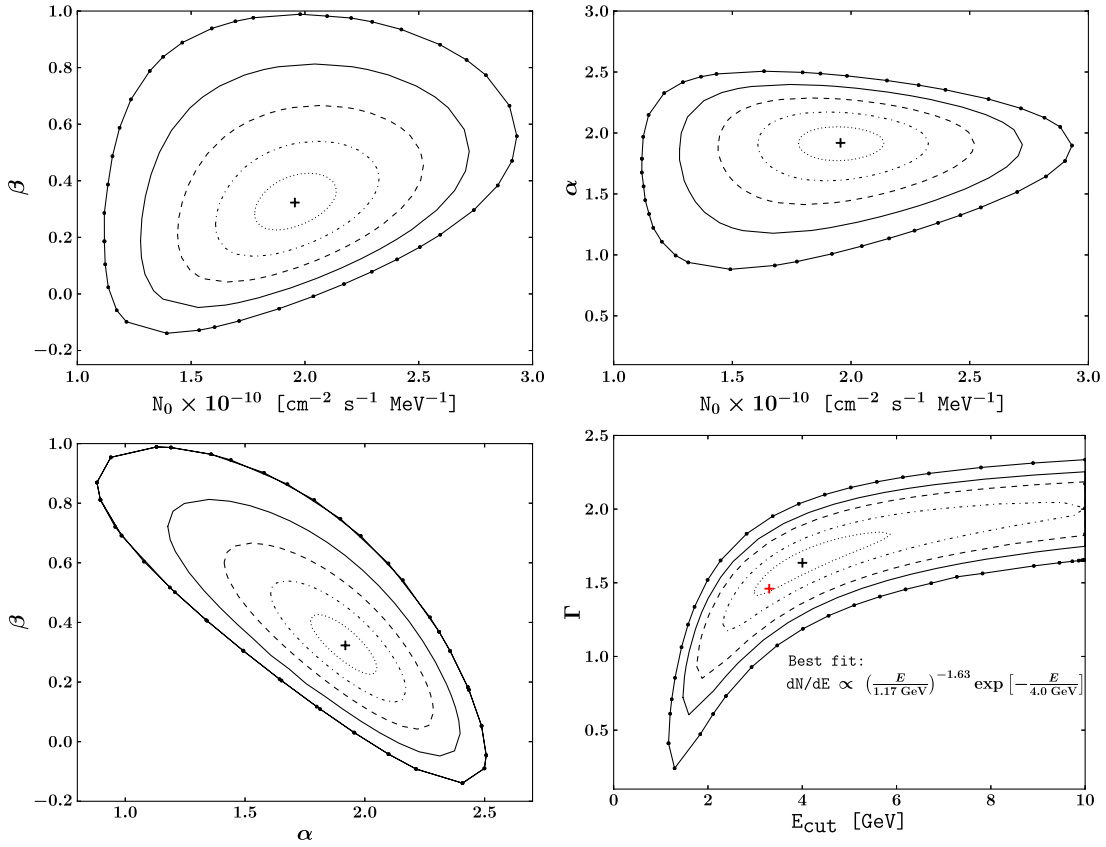

FIG. 8 (color online). Confidence regions ($1\sigma, 2\sigma, \ldots, 5\sigma$) for an unresolved population of millisecond pulsars using Fermi-LAT data taken from around the GC in the energy range 0.3–10 GeV. The spatial distribution of pulsars follows a normalized NFW profile with inner slope $\gamma = 1.2$. The two figures in the upper panel and the first one in the lower panel use a log parabola with $E_0 = 1176$ MeV for spectral shape, but the second figure in the lower panel uses an exponential cutoff as shown in the plot. Best-fit parameters are denoted by black crosses. The red cross is the best fit obtained in Ref. [45] as the average best fit of all the MSPs reported in the 2FGL catalog.

IV. RESULTS

A. Millisecond pulsars

It has been suggested [17,18] that a population of $\sim 10^3$ MSPs constitute a reasonable explanation for the gamma-ray excess seen in the GC. The main physical reasons that support this claim are the fact that MSPs can emit gamma rays over large time scales, their binary companions could prevent them from free-streaming out of the GC and estimates of the spatial distribution of the M31 low-mass X-ray binary population indicate that the number of MSPs located in the GC could scale as steeply as $1/r^{2.4}$ (with r being the two-dimensional projected radius).

To compare the spectral shape of the gamma-ray excess seen in the GC with that of typical LAT MSPs in the second-year pulsar catalog [6], we fit the LAT spectrum of the GC extended source by a power law with an exponential cutoff,

$$\frac{dN}{dE} = K\left(\frac{E}{E_0}\right)^{-\Gamma} \exp\left(-\frac{E}{E_{\rm cut}}\right), \tag{11}$$

where the photon index Γ, a cutoff energy $E_{\rm cut}$ and a normalization factor K are free parameters. The best-fit parameters, with $E_0 = 1176$ MeV, are $K = 2.5 \times 10^{-10} \pm 4 \times 10^{-11}\,{\rm ph\,cm^{-2}\,s^{-1}\,MeV^{-1}}$, $E_{\rm cut} = 4000 \pm 1500$ MeV, and $\gamma = 1.6 \pm 0.2$. The confidence regions are shown in the lower right panel of Fig. 8. It has been found in Ref. [45] that the sum of the spectra of the 37 MSPs reported in the 2FGL catalog are well described by Eq. (11) with $\Gamma = 1.46$ and $E_{\rm cut} = 3.3$ GeV [see the red cross in Fig. 8(d)]. Therefore the LAT spectrum of the extended source in the GC agrees within 1σ with what has been observed from the 37 resolved MSPs of the 2FGL.

The best-fit and confidence intervals were performed with the tool MINUIT [46]. Equation (10) was used as the goodness-of-fit statistic. Note that the 1σ contours for our two-dimensional plots correspond to the 68.3% profile likelihood [33] confidence region and are defined by all areas of the two-dimensional parameter space which have a $\Delta C_{\rm syst} \leq 2.3$, where $\Delta C_{\rm syst}$ is the difference between $C_{\rm syst}$ at the best-fit point in the plot and $C_{\rm syst}$ at the point considered for inclusion within the confidence interval.

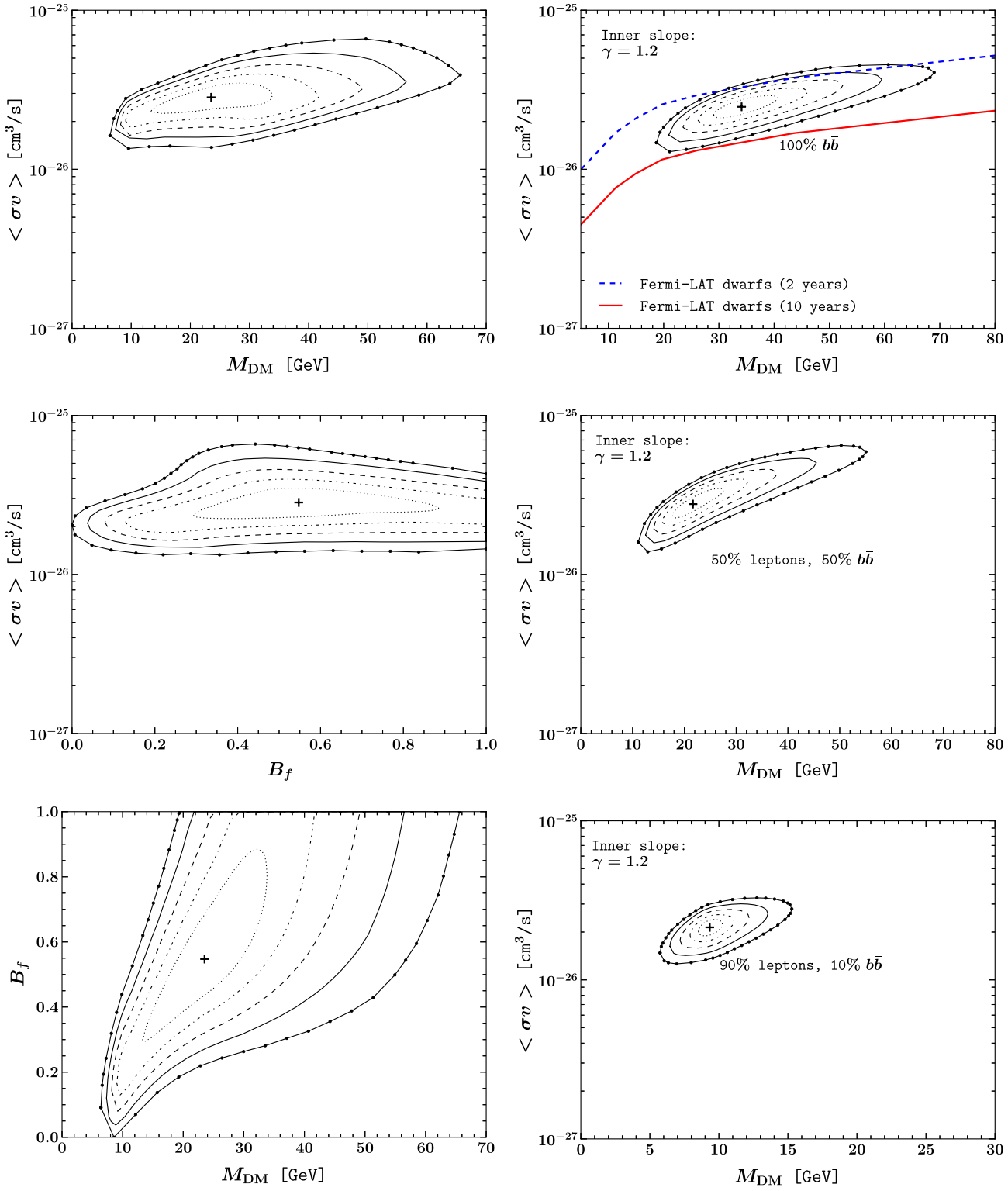

FIG. 9 (color online). Confidence regions ($1\sigma, 2\sigma, \ldots, 5\sigma$) for dark matter using Fermi-LAT data taken from around the GC in the range 0.3–10 GeV. Left panel: Best-fit $M_{\rm DM}$, $\langle\sigma v\rangle$ and B_f, and errors, marginalized over the remaining parameter. $B_f = 1.0$ implies 100% $b\bar{b}$ and $B_f = 0.0$ means 100% leptons (i.e. an unweighted combination of e^+e^-, $\mu^+\mu^-$ and $\tau^+\tau^-$ pairs). The dark matter spatial distribution follows an NFW profile with inner slope $\gamma = 1.2$. Right panel: Best-fit $M_{\rm DM}$ and $\langle\sigma v\rangle$ for several fixed values of B_f as indicated in the figures. The crosses in all frames denote the best-fit points. See Tables II and III.

All other parameters not shown in the plots are chosen to minimize $C_{\rm syst}$ at each point in the plot. The corresponding $\Delta C_{\rm syst}$ thresholds for 2, 3, 4, and 5σ are 6.2, 11.8, 19.3, and 28.7, respectively (see for example the Statistics section of Ref. [47]). For any one-parameter confidence interval we quote the 68.3% level, which corresponds to a $\Delta C_{\rm syst} = 1$ threshold.

Frames shown in the upper panel and left lower panel of Fig. 8 describe the results of a spectral fit to the LAT data using a log-parabola formula [Eq. (7)] instead of an exponential cutoff. As it can be seen, the full parameter space is shown in three two-dimensional plots. The model parameter E_0 in Eq. (7), kept fixed during the fit and set to $E_0 = 1176$ MeV, was calculated as the energy at which the relative uncertainty on the differential flux N_0 was minimal. This was done with a damping procedure that made use of the covariance matrix between parameters as obtained from the MIGRAD algorithm in MINUIT [46]. The best-fit parameters shown with black crosses in the corresponding frames of Fig. 8 are $N_0 = 1.96^{+0.18}_{-0.17} \times 10^{-10}$ ph cm^{-2} s^{-1} sr^{-1}, $\alpha = 1.92^{+0.13}_{-0.15}$ and $\beta = 0.32^{+0.10}_{-0.09}$. (For completeness, the $\pm 1\sigma$ total errors are included as well.)

In Refs. [17,18] the fit to the gamma-ray data was performed by considering statistical errors only and fixing $E_0 = 100$ MeV in the log parabola. However, we found that this choice of pivot energy produces a large correlation between the parameters N_0, α and β. We thus notice that this degeneracy can be alleviated by searching for a more adequate value of E_0, as outlined above.

B. Self-annihilating dark matter

We have seen in Figs. 3 and 4 that there is evidence for a single strong positive residual emission in the Galactic Center with a spatial morphology that agrees well with that of an NFW profile with inner slope $\gamma = 1.2$. Also, the evaluation of the systematic uncertainties related to imperfections in the Galactic diffuse background led us to the conclusion that the dark matter signals are much larger in size than the systematic errors. Thus, the next logical step is to calculate the regions of the self-annihilating DM parameter space that provide a good fit to the LAT data. In Figs. 9 and 10 we present the main results of this analysis. Contours are shown at the $1\sigma, 2\sigma, \ldots, 5\sigma$ confidence levels.

In the right upper panel of Fig. 9 we show the preferred regions of the parameter space for 100% $b\bar{b}$ final states. The 95% upper limits obtained in the Fermi-LAT analysis of dwarf galaxies [48] are also shown for comparison. We notice that the best DM region is not yet in tension with these limits. However, one would expect that the limits obtained from dwarf galaxies will be strengthened with larger data sets. We estimated that for 10 years of LAT data obtained from observations of Milky Way dwarf galaxies the 95% upper limits on $\langle \sigma v \rangle$ can be approximated to two

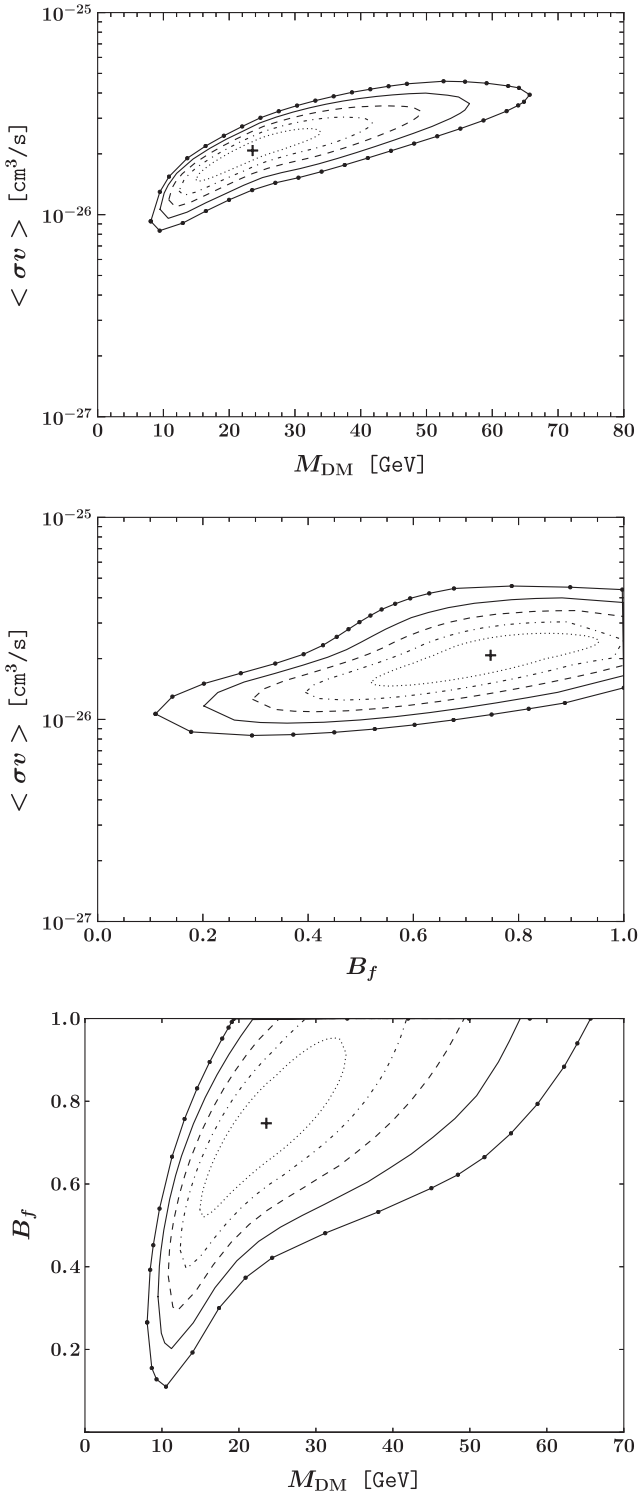

FIG. 10. Confidence regions $(1\sigma, 2\sigma, \ldots, 5\sigma)$ for dark matter using Fermi-LAT data taken from around the GC in the range 0.3–10 GeV, including best-fit $M_{\rm DM}$, $\langle \sigma v \rangle$ and B_f, and errors, marginalized over the remaining parameter. $B_f = 1.0$ implies 100% $b\bar{b}$ and $B_f = 0.0$ means 100% $\tau^+\tau^-$. The dark matter spatial distribution follows an NFW profile with inner slope $\gamma = 1.2$. The crosses in all frames denote the best-fit point. See also Table IV.

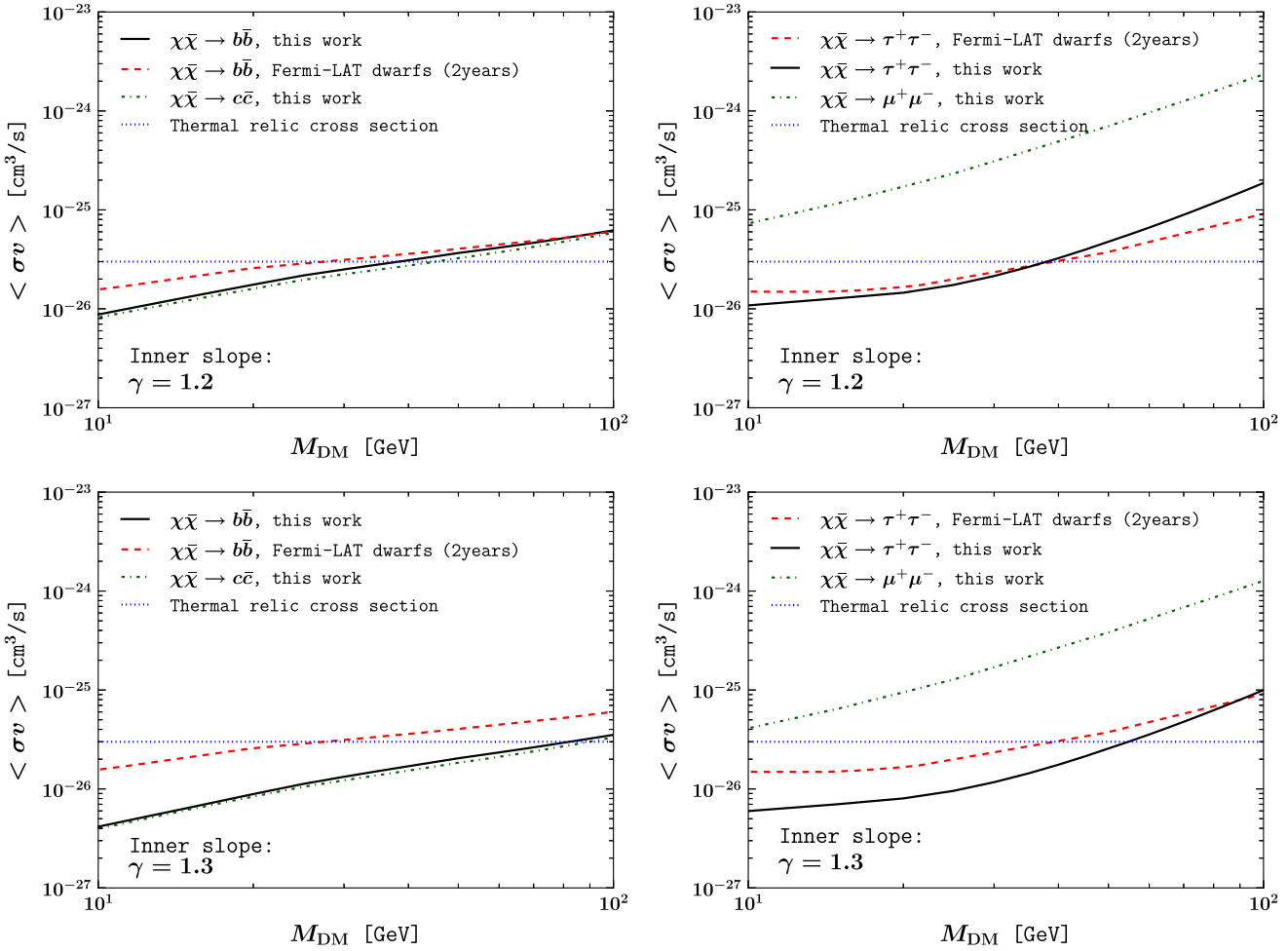

FIG. 11 (color online). Derived 95% C.L. upper limits on the velocity-averaged cross section for various annihilation channels: 100% $b\bar{b}$, 100% $c\bar{c}$, 100% $\tau^+\tau^-$ and 100% $\mu^+\mu^-$. The horizontal dotted blue line denotes the thermal decoupling cross section expected for WIMPs. Shown for comparison are the upper limits on $\langle\sigma v\rangle$ obtained from the analysis of dwarf galaxies in Ref. [48]. Limits are obtained from the analysis of 3.8 years of GC photon data in the energy range 0.3–10 GeV. Upper panel: A DM distribution given by an NFW profile with $\gamma = 1.2$ and $\rho(R_\odot) = 3.6$ GeV cm^{-3}. Lower panel: A DM distribution given by an NFW profile with $\gamma = 1.3$ and $\rho(R_\odot) = 3.4$ GeV cm^{-3}.

standard deviations of a Gaussian with a mean of zero. As the standard deviation is inversely proportional to the square root of the number of observations we can approximate the upper limits for 10 years to be $\sqrt{2/10} = 0.45$ of the upper limit of two years. (This is plotted in Fig. 9 with a red line.) We now see that our best-fit region would be ruled out by the 10-year data set. However, this is for our assumed value of $\rho_0 = 0.36$ GeV cm^{-3} and so our GC constrained $\langle\sigma v\rangle$ contours could move up or down by about 30%.

Finally, and for completeness, we present 95% C.L. upper limits on $\langle\sigma v\rangle$ from GC data in Fig. 11. Since we only used photon data in the energy range 0.3–10 GeV, we decided to compute the upper limits up to 100 GeV. We show that our derived limits are competitive with those obtained from dwarf galaxies, albeit with more uncertainty in the systematic error.

V. DISCUSSION

We find that when we include only statistical error bars in our band analysis we get best fits and errors that are a good match to those obtained using the Fermi Science Tools with the same energy range. This is a good check that our band analysis is providing an accurate representation of the data.

Using our band analysis, we could evaluate the equivalent of a TS value which includes the TS value by subtracting $C_{\rm syst}$ in Eq. (10) with $F_i^{\rm fit}$ set to the best-fit value from $C_{\rm syst}$ with $F_i^{\rm fit} = 0$. However, in this case—as the $F_i^{\rm fit} = 0$ is so far from the best fit—the Gaussian approximation, implicit in our use of the band analysis, would be expected to break down.

Although, the $\tau^+\tau^-$-only case may have $TS \gg 25$, as can be seen from Figs. 7 and 10, it does not provide a good

TABLE II. Best-fit values of the DM velocity-averaged annihilation cross section, DM mass and branching fraction when the three parameters are varied at a time. The spectra is constructed as an evenly weighted combination of $b\bar{b}$ and lepton pairs. The lepton fraction denotes an unweighted combination of e^+e^-, $\mu^+\mu^-$ and $\tau^+\tau^-$ pairs. Errors shown here include systematic uncertainties. See the left panel of Fig. 9 for further details.

Best-fit branching ratio	$\langle\sigma v\rangle$ [cm^3/s]	$M_{\rm DM}$ [GeV]
$55^{+18}_{-16}\%$ $b\bar{b}$	$2.84^{+0.43}_{-0.41}\times10^{-26}$	$23.5^{+6.7}_{-6.6}$

TABLE III. Best-fit $M_{\rm DM}$ and $\langle\sigma v\rangle$ for several fixed values of B_f. The lepton fraction denotes an unweighted combination of e^+e^-, $\mu^+\mu^-$ and $\tau^+\tau^-$ pairs. Errors shown here include systematic uncertainties. See the right panel of Fig. 9 for further details.

Branching ratio	$\langle\sigma v\rangle$ [cm^3/s]	$M_{\rm DM}$ [GeV]
100% $b\bar{b}$	$2.47^{+0.28}_{-0.25}\times10^{-26}$	$34.1^{+4.0}_{-3.5}$
50% $b\bar{b}$, 50% leptons	$2.77^{+0.47}_{-0.35}\times10^{-26}$	$21.7^{+3.8}_{-2.8}$
10% $b\bar{b}$, 90% leptons	$2.14^{+0.17}_{-0.16}\times10^{-26}$	$9.3^{+0.6}_{-0.5}$

TABLE IV. Best-fit values of the DM velocity-averaged annihilation cross section, DM mass and branching fraction when the three parameters are varied at a time. The spectra is constructed as an unweighted combination of $b\bar{b}$ and $\tau^+\tau^-$ pairs. Errors shown here include systematic uncertainties. See Fig. 10 for further details.

Best-fit branching ratio	$\langle\sigma v\rangle$ [cm^3/s]	$M_{\rm DM}$ [GeV]
$75^{+13}_{-15}\%$ $b\bar{b}$	$2.1^{+0.27}_{-0.45}\times10^{-26}$	$23.6^{+6.7}_{-6.4}$

fit to the data. References [16–18] provide analysis of the $\tau^+\tau^-$ as an acceptable model. Although we agree that the $\tau^+\tau^-$ with $M\approx10$ GeV does provide a good TS value, we have shown that it provides a poor fit to the data. Similarly, as can be seen from Fig. 9, a pure lepton spectrum does not provide a good fit to the data. However, as can be seen from Figs. 9, 7, and 10, a $b\bar{b}$-only spectrum does provide a good fit. In Refs. [17,18] a fit for a range of masses for a $b\bar{b}$ model was obtained. For their Fermi Science Tools analysis they find that models with $10\leq M_{\rm DM}\leq110$ have $TS\geq25$. Using the same data and method we have reproduced their constraints on $\langle\sigma v\rangle$ in Fermi Tools. However, as we see from Fig. 9, only $b\bar{b}$ models with $20\leq M_{\rm DM}\leq60$ GeV are within the 4σ confidence region. This shows that despite the fact that models such as $M_{\rm DM}=10$ GeV provide a good TS value, they do not provide a good fit to the data, as can also be seen in Fig. 7.

If the WIMPs are Majorana fermions, then the pair annihilation into light fermions is highly suppressed since the invariant scattering amplitude $|\mathcal{M}|^2\propto m_f^2$ [49]. Furthermore, if annihilations into gauge bosons are also suppressed and the WIMPs are lighter than the top quark then the prevailing annihilation final states are $b\bar{b}$ and $\tau^+\tau^-$. By virtue of the color charge of the bottom quarks [49], one would expect the production of $b\bar{b}$ pairs to be typically more than three times larger than those of $\tau^+\tau^-$. Thus, we note that one could easily accommodate a theoretical model to these findings.

The best-fit DM models (see Tables II, III, and IV, and Figs. 9 and 10) have values for $\langle\sigma v\rangle$ intriguingly close to the simple thermal relic value. An even closer match is obtained from a more precise WIMP relic abundance cross section of $\langle\sigma v\rangle=2.2\times10^{-26}$ cm^3 s^{-1}, which has a feeble mass dependence for masses above 10 GeV [50].

Our SEDs are designed to be of the GC extended emission component only, while those of Ref. [16] also include Sgr A* and a component known as the HESS ridge, which we will discuss later in this section. Also, comparing our results with Ref. [16] is difficult as they used a profile with a slope $\rho\propto r^{-\gamma}$ rather than a generalized NFW profile, as in Eq. (6). For a generalized NFW profile the line-of-sight integral, Eq. (4), formally extends to an infinite distance from the observer. Because of the steep dropoff beyond r_s, the integral is insensitive to the actual upper bound used provided it is much larger than r_s. However, if only the inner slope is used then the J factor depends sensitively on the assumed upper bound, and an upper bound of ∞ would give much too large an answer. Unfortunately, the range of the line-of-sight integral used for the Galactic Center results of Ref. [16] is not provided and so we are unable to reliably compare our constraints with theirs for $\langle\sigma v\rangle$. But, interestingly, our constraints for the $\gamma=1.3$ case are a good match with theirs; see Figs. 11 and 12. For the $\gamma=1.3$ case, the value of ρ_0 determined by maximizing the likelihood of the microlensing and dynamical data (see Fig. 5 of Ref. [34]) with $\gamma=1.3$ is $\rho_0=0.34$ GeV cm^{-3}. Our ρ_0 for $\gamma=1.2$ and $\gamma=1.3$ match the corresponding ρ_0 in Ref. [16]. But, without the upper limit for their line-of-sight integral, it is not clear whether this match is coincidental or not. Note that in the upper-limits plot of Fig. 12, the match is not as good for $M_{\rm DM}>100$ GeV, but this is likely due to the fact that in their corresponding plot they used their 10 to 100 GeV bin and for $M_{\rm DM}>100$ GeV the DM spectrum significantly overlaps with this region.

For $\gamma=1.2$ the match is not as good; see Fig. 12. As Fig. 2 shows, the inner PSs are very degenerate with the excess emission component and in the GC analysis of Ref. [16] they used the 2FGL parameters for all the PSs except Sgr A*, which they fit with a PS to the data without a GC excess emission component. Their Sgr A* fit (see Fig. 4 of Ref. [16]) is very similar to ours for the baseline model in Fig. 2. They did use a broken power-law parametrization rather than a log parabola, but this difference has a negligible effect. So their analysis does not utilize the degeneracy between the PSs—especially Sgr A*—and

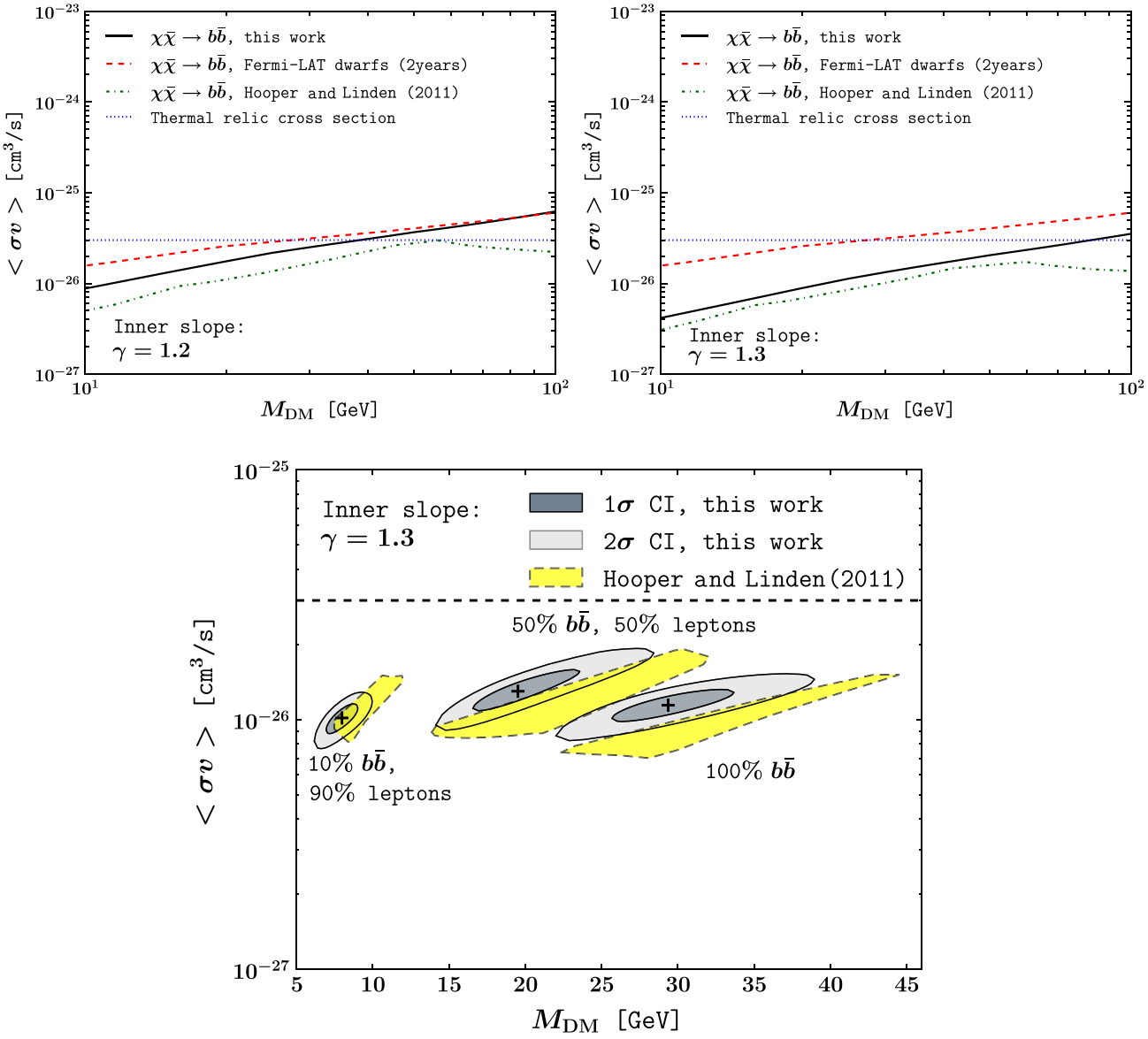

FIG. 12 (color online). Upper panel: Shown are the 95% C.L. upper limits on the velocity-averaged cross section for 100% $b\bar{b}$ final states. The horizontal dotted blue line denotes the thermal decoupling cross section expected for WIMPs. Shown for comparison are the upper limits obtained from the analysis of dwarf galaxies in Ref. [48] and the GC analysis in Ref. [16] (see more details in Fig. 11). Lower panel: Shown are the regions of the parameter space which provide a good fit to Fermi-LAT data as derived in this work (grey area) and in Hooper *et al.* [16] (yellow area).

the GC excess emission component. This implies that the analysis of Ref. [16] will have a suppressed dark matter $\langle\sigma v\rangle$ when compared to ours.

In Ref. [51] a generalized NFW profile was used, but there they dis not account for Sgr A* as they were seeking a robust upper limit to the DM cross section. They also chose values of γ and ρ_0 consistent with the microlensing and dynamical data [34], but they were chosen to be conservative with respect to a potential dark matter annihilation signal. Consistent with this, their upper limits are larger than ours. Also, again the match is more discrepant for $M_{\rm DM} > 100$ GeV, but this is likely due to the fact that they used the 10 to 100 GeV data range, and for $M_{\rm DM} > 100$ GeV the DM spectrum significantly overlaps with this energy region.

In the GC analysis of Ref. [16], they investigated adding a HESS Galactic Ridge component [52]. The 2 by 1 degree HESS Galactic Ridge was measured by HESS over the energy range 0.2 to 10 TeV. It was found to be spatially correlated with the molecular clouds in the central 200 parsecs of the Milky Way. Its origin is usually taken to be the decays of neutral pions produced in the interactions of a harder than usual population of cosmic-ray protons and nuclei with the surrounding molecular gas. In Ref. [16]

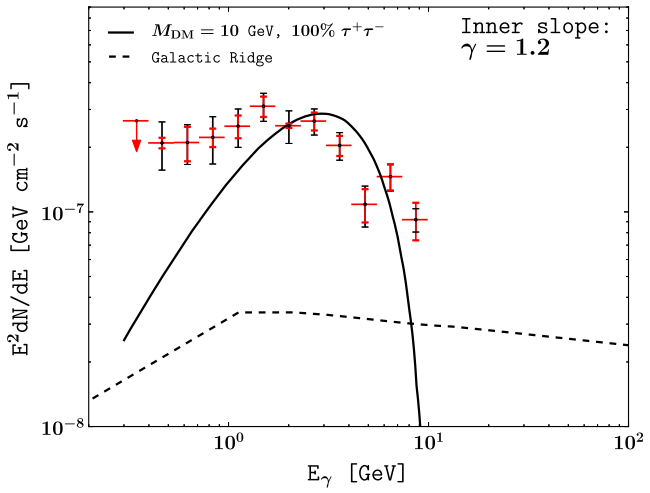

FIG. 13 (color online). SED of the extended source assuming an NFW profile with $\gamma = 1.2$ and $\rho(R_\odot) = 0.36$ GeV cm^{-3}. The best-fit spectrum obtained with $M_{DM} = 10$ GeV and 100% $\tau^+\tau^-$ final states is overlaid over the twelve energy-flux data points. Red error bars represent systematic errors and black error bars represent statistical errors. For illustration we also plot the spectra of the Galactic Ridge as obtained in Fig. 7 of Ref. [16], but this source was not considered in our actual fits. See the text for a discussion on this.

they evaluated the spectrum for this model at energies less than 100 GeV and used this in their model fit.

As can be seen from Fig. 13, the HESS ridge postulated by Ref. [16] should not significantly affect the fit in our case. This is because we are using $\gamma = 1.2$, which leads to a higher inferred DM flux, and also we are refitting our PSs which allows the DM flux to be higher by lowering the emission of the PSs close to the GC.

The GC excess emission results of Ref. [53] are quoted as being derived from a generalized NFW which is effectively equivalent to the one we are using for $\gamma = 1.2$, albeit with a density of $\rho_0 = 0.4$ GeV/cm^3. But, as they did not simultaneously fi their PS and DM models, this likely explains why they found a significantly smaller value for $\langle\sigma v\rangle = 8 \times (0.4/0.36)^2 \times 10^{-27} = 9.9 \times 10^{-27}$ cm^3 s^{-1} for the $M_{DM} = 50$ GeV (100% $b\bar{b}$) case for $\gamma = 1.2$. We have converted their value to the equivalent value for our assumed local density. As can be seen from the top left plot in Fig. 9, this is outside our 5σ confidence region. However, if instead of taking the best fit ρ_0 from the microlensing and dynamical data (see Fig. 5 of Ref. [34]) one sees how the result changes if one takes the contour 68% limits, $\rho_0 \in [0.3, 0.4]$, the error for $\langle\sigma v\rangle$ becomes of order 20%, taking into account the ρ_0^2 dependence of the J factor shown in Eq. (4). However, this is only important in estimating $\langle\sigma v\rangle$ and does not affect statements like how a 10 GeV DM annihilating only to $\tau^+\tau^-$ does not provide a good fit to the Fermi-LAT data, as the goodness of fit to the gamma-ray data is independent of $\langle\sigma v\rangle$ due to the complete degeneracy between $\langle\sigma v\rangle$ and ρ_0^2.

In Ref. [16], they stated that they included the observed spatial variations of the residuals as a systematic error. Details were not given on the magnitude, while in an earlier related paper [14] a value of 3% is given. By varying the parameters used in GALPROP for the distribution of cosmic rays, interstellar gas and radiation fields, the Fermi-LAT team reported a systematic error of order 10% for the inner Galaxy and for energies less than 10 GeV, with unresolved point sources being cited as a likely cause [43]. Reference [15] found systematic errors of about 10% in a 2° area around the GC by doing Monte Carlo simulations of a model with no GC diffuse source. Thus, overall our estimate of 20% is higher than other estimates.

Our confidence regions for MSPs are in good agreement with the average pulsar spectrum measured by Fermi-LAT; see Fig. 8. For the pulsar hypothesis, it is interesting to evaluate the number of MSPs needed to account for the excess emission. For an energy range of 100 MeV to 10 GeV, Ref. [54] found that 47 Tuc had a flux of $2.6(\pm 0.8) \times 10^{-8}$ photons cm^{-2} s^{-1}. Also, 47 Tuc is 4 kpc away and the integration time was 194.3 days. We take the Galactic Center to be 8.25 kpc and our integration time is 3.8 years. The population of MSPs in 47 Tuc is taken to be 30 to 60. Therefore, taking the flux to be proportional to the number of MSPs multiplied by the integration time and the inverse square of the distance, the equivalent flux of one pulsar in our Galactic Center for our time period in the energy range 100 MeV to 10 GeV is between 1.5×10^{-9} and 7.3×10^{-10} ph cm^{-2} s^{-1}. The flux of our best-fit exponential cutoff in the energy range 100 MeV to 10 GeV is obtained by integrating the parametric form of Eq. (11) with the best-fit parameters quoted in Sec. IV A, and it is found to be 1.7×10^{-6} ph cm^{-2} s^{-1}. Therefore we find the number of MSPs needed to explain the GC excess emission to be between 1100 and 2100, which is a similar to what Refs. [17,18] found.

However, if the excess extended emission was also responsible for the bulk of the low-latitude, low-energy emission of the Fermi bubbles—as was suggested in Ref. [53]—the spectral and spatial properties typical of a population of MSPs would not be a good fit to the signal [45].

References [17,18] also examined a proposal by Ref. [22] which entails high-energy cosmic-ray electrons producing bremsstrahlung gamma rays on molecular gas. This case can have a significant effect on the spatial emission. Reference [22] found that the source electron population is consistent with radio observations of synchrotron emission from the high-energy population of electrons, as well as the morphology of the FeI 6.4 keV X-ray emission. References [17,18] found that by using the radio emission morphology, tracing the synchrotron emission from the cosmic-ray electrons improves the fit over the

base model with a $TS = 252$ for an energy range of 1 to 100 GeV. But this was significantly smaller than what they obtained for a log-parabola spectrum for the same energy range, which gave $TS = 412$.

This indicates that the bremsstrahlung model may not be providing a good fit, in much the same way as we have found that $\tau^+\tau^-$ has a good TS but not as good as $b\bar{b}$, which was a good fit.

VI. CONCLUSIONS

We have found that either a DM annihilation model or an unresolved pulsar population is consistent with the observed excess gamma-ray emission seen in the GC. Our analysis was marginalized over the PS and diffuse background amplitudes in the region of interest. We included an estimated systematic error for the diffuse galactic background of about 20%. We provided confidence regions for the model parameters.

We found that a population of 1000–2000 MSPs with parameters consistent with the average spectral shape of Fermi-LAT measured MSPs was able to fit the GC excess emission. For DM, we found that a pure $\tau^+\tau^-$ annihilation channel is not a good fit to the data. But a mixture of $\tau^+\tau^-$ and $b\bar{b}$ with $\langle\sigma v\rangle$ of order the thermal relic value and a DM mass of around 20 to 60 GeV provides an adequate fit.

ACKNOWLEDGMENTS

We thank Kev Abazajian, Jenni Adams, Terri Brandt, Tim Cohen, Dan Hooper, Junichiro Katsuta, Tim Linden, Gavin Rowell, Tracy Slatyer, and Johann Cohen-Tanugi for helpful discussions. We also thank the Fermi Collaboration for making the Fermi-LAT data and Fermi Science Tools so readily available. O. M. especially expresses his thanks to Stefano Profumo for allowing him to study the original Fortran version of the DMFIT package. O. M. is supported by a UC Doctoral Scholarship.

APPENDIX: GAMMA-RAY EXCESS DATA

TABLE V. Summary of spectral data, statistical errors and systematic errors used in our analysis. A graphical representation of this data can be found in Fig. 7. The spectral point dN/dE evaluated at the logarithmic midpoint of $E_{\mathrm{min,i}}$ and $E_{\mathrm{max,i}}$ has been evaluated from F_i using $dN/dE \approx \frac{F_i}{(E_{\mathrm{max,i}} - E_{\mathrm{min,i}})}$. Since the first band (0.30–0.40 GeV) had a $TS < 10$ we report a 2σ upper limit instead.

E_{min} [GeV]	E_{max} [GeV]	dN/dE [GeV^{-1} cm^{-2} s^{-1}]	Statistical error [GeV^{-1} cm^{-2} s^{-1}]	Systematic error [GeV^{-1} cm^{-2} s^{-1}]
0.30	0.40	2.20×10^{-6}	—	—
0.40	0.54	9.69×10^{-7}	5.52×10^{-8}	2.45×10^{-7}
0.54	0.72	5.43×10^{-7}	9.89×10^{-8}	1.14×10^{-7}
0.72	0.97	3.20×10^{-7}	3.16×10^{-8}	7.94×10^{-8}
0.97	1.29	2.01×10^{-7}	2.44×10^{-8}	4.08×10^{-8}
1.29	1.73	1.39×10^{-7}	1.51×10^{-8}	2.07×10^{-8}
1.73	2.32	6.27×10^{-8}	1.48×10^{-9}	1.09×10^{-8}
2.32	3.11	3.67×10^{-8}	3.52×10^{-9}	5.11×10^{-9}
3.11	4.16	1.58×10^{-8}	1.69×10^{-9}	2.32×10^{-9}
4.16	5.57	4.67×10^{-9}	8.28×10^{-10}	1.01×10^{-9}
5.57	7.47	3.51×10^{-9}	4.82×10^{-10}	5.03×10^{-10}
7.47	10.00	1.23×10^{-9}	2.46×10^{-10}	1.53×10^{-10}

[1] G. Bertone, D. Hooper, and J. Silk, Phys. Rep. **405**, 279 (2005).
[2] M. Cirelli, Pramana **79**, 1021 (2012).
[3] D. Clowe, M. Bradač, A. H. Gonzalez, M. Markevitch, S. W. Randall, C. Jones, and D. Zaritsky, Astrophys. J. **648**, L109 (2006).
[4] T. Bringmann and C. Weniger, Phys. Dark Univ. **1**, 194 (2012).
[5] E. A. Baltz *et al.*, J. Cosmol. Astropart. Phys. 07 (2008) 013.
[6] P. L. Nolan *et al.*, Astrophys. J. Suppl. Ser. **199**, 31 (2012).
[7] T. Linden, E. Lovegrove, and S. Profumo, Astrophys. J. **753**, 41 (2012).
[8] A. Geringer-Sameth and S. M. Koushiappas, Phys. Rev. Lett. **107**, 241303 (2011).

[9] M. Ackermann *et al.* (Fermi-LAT Collaboration), Phys. Rev. Lett. **107**, 241302 (2011).
[10] S. Ando and D. Nagai, J. Cosmol. Astropart. Phys. 07 (2012) 017.
[11] J. Han, C. S. Frenk, V. R. Eke, L. Gao, S. D. M. White, A. Boyarsky, D. Malyshev, and O. Ruchayskiy, Mon. Not. R. Astron. Soc. **427**, 1651 (2012).
[12] O. Macías, C. Gordon, A. M. Brown, and J. Adams, Phys. Rev. D **86**, 076004 (2012).
[13] L. Goodenough and D. Hooper, arXiv:0910.2998.
[14] D. Hooper and L. Goodenough, Phys. Lett. B **697**, 412 (2011).
[15] A. Boyarsky, D. Malyshev, and O. Ruchayskiy, Phys. Lett. B **705**, 165 (2011).
[16] D. Hooper and T. Linden, Phys. Rev. D **84**, 123005 (2011).
[17] K. N. Abazajian and M. Kaplinghat, Phys. Rev. D **86**, 083511 (2012).
[18] K. N. Abazajian and M. Kaplinghat, Phys. Rev. D **87**, 129902 (2013).
[19] V. Vitale and A. Morselli (Fermi-LAT Collaboration), arXiv:0912.3828.
[20] V. Vitale and A. Morselli (Fermi-LAT Collaboration), Nucl. Instrum. Methods Phys. Res., Sect. A **630**, 147 (2011).
[21] K. N. Abazajian, J. Cosmol. Astropart. Phys. 03 (2011) 010.
[22] F. Yusef-Zadeh *et al.*, Astrophys. J. **762**, 33 (2013).
[23] M. Ackermann *et al.* (Fermi-LAT Collaboration), Astrophys. J. Suppl. Ser. **203**, 4 (2012).
[24] J. R. Mattox *et al.*, Astrophys. J. **461**, 396 (1996).
[25] S. S. Wilks, Ann. Math. Stat. **9**, 60 (1938).
[26] J. Han, C. S. Frenk, V. R. Eke, L. Gao, and S. D. M. White, arXiv:1201.1003.
[27] J. Han, C. S. Frenk, V. R. Eke, L. Gao, S. D. M. White, A. Boyarsky, D. Malyshev, and O. Ruchayskiy, Mon. Not. R. Astron. Soc. **427**, 1651 (2012).
[28] E. A. Baltz *et al.*, J. Cosmol. Astropart. Phys. 07 (2008) 013.
[29] C. Rott, Nucl. Phys. B, Proc. Suppl. **235–236**, 413 (2013).
[30] L. Bergstrom, P. Ullio, and J. H. Buckley, Astropart. Phys. **9**, 137 (1998).
[31] J. F. Navarro, C. S. Frenk, and S. D. M. White, Astrophys. J. **462**, 563 (1996).
[32] A. Klypin, H. Zhao, and R. S. Somerville, Astrophys. J. **573**, 597 (2002).
[33] W. A. Rolke, A. M. López, and J. Conrad, Nucl. Instrum. Methods Phys. Res., Sect. A **551**, 493 (2005).
[34] F. Iocco, M. Pato, G. Bertone, and P. Jetzer, J. Cosmol. Astropart. Phys. 11 (2011) 029.
[35] T. E. Jeltema and S. Profumo, J. Cosmol. Astropart. Phys. 11 (2008) 003.
[36] P. Gondolo, J. Edsjö, P. Ullio, L. Bergström, M. Schelke, and E. A. Baltz, J. Cosmol. Astropart. Phys. 07 (2004) 008.
[37] T. Sjostrand, S. Mrenna, and P. Z. Skands, J. High Energy Phys. 05 (2006) 026.
[38] J. A. R. Cembranos, A. de la Cruz-Dombriz, V. Gammaldi, R. A. Lineros, and A. L. Maroto, J. High Energy Phys. 09 (2013) 077.
[39] T. Sjostrand, S. Mrenna, and P. Z. Skands, Comput. Phys. Commun. **178**, 852 (2008).
[40] M. Cirelli, G. Corcella, A. Hektor, G. Hütsi, M. Kadastik, P. Panci, M. Raidal, F. Sala, and A. Strumia, J. Cosmol. Astropart. Phys. 03 (2011) 051.
[41] M. Kachelriess, P. D. Serpico, and M. A. Solberg, Phys. Rev. D **80**, 123533 (2009).
[42] P. Ciafaloni, D. Comelli, A. Riotto, F. Sala, A. Strumia, and A. Urbano, J. Cosmol. Astropart. Phys. 03 (2011) 019.
[43] M. Ackermann *et al.*, Astrophys. J. **750**, 3 (2012).
[44] A. A. Abdo *et al.*, Astrophys. J. **722**, 1303 (2010).
[45] D. Hooper, I. Cholis, T. Linden, J. Siegal-Gaskins, and T. Slatyer, arXiv:1305.0830 [Phys. Rev. D (to be published)].
[46] F. James and M. Roos, Comput. Phys. Commun. **10**, 343 (1975).
[47] J. Beringer *et al.* (Particle Data Group), Phys. Rev. D **86**, 010001 (2012).
[48] M. Ackermann *et al.* (Fermi-LAT collaboration), Phys. Rev. Lett. **107**, 241302 (2011).
[49] S. Profumo, arXiv:1301.0952.
[50] G. Steigman, B. Dasgupta, and J. F. Beacom, Phys. Rev. D **86**, 023506 (2012).
[51] D. Hooper, C. Kelso, and F. S. Queiroz, Astropart. Phys. **46**, 55 (2013).
[52] F. Aharonian *et al.*, Nature (London) **439**, 695 (2006).
[53] D. Hooper and T. R. Slatyer, Phys. Rev. D **88**, 043513 (2013).
[54] A. A. Abdo *et al.*, Science **325**, 845 (2009).